

Primordial non-Gaussian signatures in CMB polarization

This content has been downloaded from IOPscience. Please scroll down to see the full text.

JCAP02(2015)028

(<http://iopscience.iop.org/1475-7516/2015/02/028>)

View [the table of contents for this issue](#), or go to the [journal homepage](#) for more

Download details:

IP Address: 169.237.46.240

This content was downloaded on 20/04/2016 at 00:46

Please note that [terms and conditions apply](#).

Primordial non-Gaussian signatures in CMB polarization

Vidhya Ganesan,^a Pravabati Chingangbam,^a K.P. Yogendran^b
and Changbom Park^c

^aIndian Institute of Astrophysics,
Koramangala II Block, Bangalore 560 034, India

^bIndian Institute of Science Education and Research,
Sector 81, Mohali, India

^cKorea Institute for Advanced Study,
85 Hoegiro, Dongdaemun-gu, Seoul 130-722, Korea

E-mail: vidhya@iiap.res.in, prava@iiap.res.in, yogendran@iisermohali.ac.in,
cbp@kias.re.kr

Received November 21, 2014

Revised January 23, 2015

Accepted January 28, 2015

Published February 23, 2015

Abstract. We study the signatures of local type primordial non-Gaussianity, parametrized by f_{NL} , of scalar perturbations in CMB polarization using the probability distribution functions, Minkowski Functionals and Betti numbers. We show that the lowest order non-Gaussian deviation of the PDF of the total polarization intensity is at order $(f_{\text{NL}}\sigma)^2$. We calculate the non-Gaussian deviations of Minkowski Functionals and Betti numbers from simulated polarization maps. If observational issues such as instrumental noise are ignored, we find that E mode polarization provides independent and equally strong constraint on f_{NL} as temperature fluctuations. The constraint is expected to weaken when observational issues are included since the signal-to-noise ratio of polarization data is lower than that of temperature. The non-Gaussian signal in the total polarization intensity, however, is much weaker and has a relatively large cosmic variance and hence may not be useful for detecting local type non-Gaussianity.

Keywords: CMBR polarisation, non-gaussianity

ArXiv ePrint: [1411.5256](https://arxiv.org/abs/1411.5256)

Contents

1	Introduction	1
2	Local type primordial non-Gaussianity, polarization fields and simulations	2
3	Probability distribution functions and non-Gaussian deviations	3
4	Geometrical and topological observables	6
4.1	Non-Gaussian deviations of Minkowski Functionals	8
4.2	Non-Gaussian deviations of Betti numbers	11
4.3	Comparison of statistical sensitivity of T , E and \tilde{I} to primordial non-Gaussianity	11
5	Conclusion	13

1 Introduction

The Cosmic Microwave Background radiation photons are polarized [1–5] at less than 10% level due to quadrupolar anisotropies that were present in the plasma before the epoch of matter and radiation decoupling. The detection of this polarization is extremely valuable and will enhance our knowledge about the universe by providing a consistency check of the standard cosmological model that has been inferred from temperature fluctuations and improve constraints on the cosmological parameters. Inflation [6–10] predicts that the amplitude and phase of the fluctuations in the energy density during the very early stages of the Universe are random variables with a nearly Gaussian probability distribution function. Their precise statistical nature, in particular the manner of deviation from Gaussianity, has been the subject of intense study during the past decade. All models of inflation, in general, predict some amount of deviation of these fluctuations from a Gaussian distribution. The details of the deviations are model dependent making it possible to discriminate different theoretical models using present day observations.

The statistical nature of the primordial fluctuations are imprinted on the fluctuations in the CMB temperature and polarization, and matter distributions. Observations of these fluctuations enable us to reconstruct features of the primordial fluctuations. Searches for primordial non-Gaussianity have so far focused on using the fluctuations in the CMB temperature. Some of these searches use geometrical and topological observables associated with excursion sets. Of these, probably the most widely used are the Minkowski Functionals [11–16]. They have been applied to observational data of temperature fluctuations to constrain primordial non-Gaussianity [17–20] and also to identify traces of residual foreground contamination [21]. Other such observables include clustering strength of the excursion set [22–24], number counts of hot and cold spots (or Betti numbers) [25–30] and extrema counts [31]. Studies on Betti numbers and extrema counts for the CMB have been theoretical nature and have not yet been applied to observational data.

In this work, we focus on the so-called local type primordial non-Gaussianity which is parametrized by the parameter f_{NL} [32–35]. We extend the study of Minkowski Functionals and Betti numbers to the polarization field. Previous analysis of polarization along these lines can be found in [36, 37]. We calculate the effects of primordial non-Gaussianity on the

polarization signal and compare them with what is obtained for the temperature fluctuations focusing on scalar density fluctuations generated during inflation. From temperature data, the current constraints on f_{NL} given by PLANCK data [20] is $f_{\text{NL}} = 2.7 \pm 5.8$ at 68% CL. Recently, Galli et al. [38] showed that polarization data can vastly improve constraints on cosmological parameters in comparison to using temperature data alone. Our work in this paper is along similar lines and we investigate the shapes and amplitudes of non-Gaussian deviations that show up in Minkowski Functionals and Betti numbers for the polarization fields, compare them with deviations seen for temperature fluctuations and comment on their power to constrain f_{NL} . We do not address real observational issues such as instrument noise, incomplete sky, beam shapes, etc. and study the non-Gaussian signal relative to the cosmic variance.

This paper is organized as follows. In section 2, we briefly describe local type primordial non-Gaussianity and non-Gaussian simulations. In section 3 we present analytic expressions and numerical calculations from simulations of the Gaussian and non-Gaussian probability distribution functions of E and I . In section 4, we describe Minkowski Functionals and Betti numbers and their numerical calculation. Then we present our results for non-Gaussian deviations of these observables. Further, we perform a simple comparison of the statistical sensitivity of the primordial non-Gaussian information encoded in temperature fluctuations and polarization using the deviations of Minkowski Functionals. We end by summarizing the results along with a discussion of their implications in section 5.

2 Local type primordial non-Gaussianity, polarization fields and simulations

In the local type primordial non-Gaussianity the primordial gravitational potential Φ takes the form

$$\Phi(\mathbf{x}) = \Phi^G(\mathbf{x}) + f_{\text{NL}} \left\{ (\Phi^G(\mathbf{x}))^2 - \langle (\Phi^G)^2 \rangle \right\}, \quad (2.1)$$

where Φ^G is Gaussian and f_{NL} is a constant parameter that quantifies the extent of non-Gaussianity. The expression is meaningful for values of f_{NL} small enough so that the second term is smaller compared to the first. Φ sets the initial conditions in the theoretical calculation of temperature fluctuations and polarization.

The two degrees of freedom of polarization are encoded in the Stokes parameters Q and U . These transform as spin 2 objects under rotations along the line of sight. They can be re-expressed in terms of the curl-free and divergence free components, the so-called E and B modes [39, 40]. E is a scalar and B is a pseudo-scalar. E modes have been observationally detected by DASI [41] and subsequently by WMAP [42]. For our analysis in this paper we use the E -mode and the total polarization intensity, defined as $I \equiv \sqrt{Q^2 + U^2}$. In general, Q and U contain independent information. Here we consider the case where B mode is absent (the tensor-to-scalar ratio, r being zero). Under this condition Q and U are correlated and E mode contains the full information in the two modes.

We use simulations of temperature fluctuations and E mode polarization with input primordial fluctuations of the form given by eq. (2.1) that have been made publicly available by Elsner and Wandelt [43]. The simulations follow the algorithm given in [44] and involve calculating $a_{\ell m}^i$ where i can be either $\Delta T/T_{\text{CMB}}$ or E . $a_{\ell m}^i$ is obtained from

$$\begin{aligned} a_{\ell m}^i &= \int dr r^2 \Phi_{\ell m}(r) \Delta_{\ell}^i(r) \\ &= \int dr r^2 \Phi_{\ell m}^G(r) \Delta_{\ell}^i(r) + \int dr r^2 \Phi_{\ell m}^{\text{NG}}(r) \Delta_{\ell}^i(r), \end{aligned} \quad (2.2)$$

where $\Delta_\ell^i(r)$ is the transfer function for the respective i , and $\Phi_{\ell m}(r)$ is the harmonic transform of $\Phi(\mathbf{x})$ with Gaussian and non-Gaussian parts denoted by Φ^G and Φ^{NG} . For expressions relating $\Phi(\mathbf{x})$ and $\Phi_{\ell m}(r)$ we refer to [44]. The fields $\Delta T/T_{\text{CMB}}$ or E are obtained by performing harmonic transform of the respective $a_{\ell m}^i$'s. A similar algorithm was applied to generate maps of temperature fluctuations for cubic order perturbations of Φ [45]. The differences in the maps of $\Delta T/T_{\text{CMB}}$ and E arise from different physical effects encoded in their respective transfer functions.

The simulations have resolution set by the maximum multipole $\ell_{\text{max}} = 1024$ and the HEALPIX variable $n_{\text{side}} = 512$. The input cosmological parameters are those obtained from WMAP5+BAO+SN data given in [46]. We consider Gaussian smoothing of the input maps to study the non-Gaussian effects at different resolutions parametrized by smoothing angles θ_s . Note that θ_s is related to the FWHM as $\theta_s = \text{FWHM}/\sqrt{8 \ln 2}$.

For the calculations of Minkowski Functionals and Betti numbers we use the mean shifted total polarization intensity denoted by

$$\tilde{I} \equiv I - \langle I \rangle. \quad (2.3)$$

3 Probability distribution functions and non-Gaussian deviations

The statistical properties of the primordial gravitational potential are directly reflected in $\Delta T/T_{\text{CMB}}$ and E provided the perturbations evolve linearly during subsequent epochs. This implies that if the probability distribution function (PDF) of Φ is Gaussian then the PDF of $\Delta T/T_{\text{CMB}}$ and E will also be Gaussian [1]. On the other hand if the PDF has a non-Gaussian form then $\Delta T/T_{\text{CMB}}$ and E will trace the same distribution. Similarly, Q and U will trace the PDF of Φ , which in turn will lead to the PDF for I .

Let P denote the PDF for a generic field. We first derive P , for a field which has the form of eq. (2.1) and whose Gaussian part is denoted by X . The expectation value of a function $f(X + f_{\text{NL}}(X^2 - \sigma^2))$, where $\sigma^2 = \langle X^2 \rangle$, may be computed using the Fourier transform as

$$\langle f \rangle = \int dX P(X) f(X + f_{\text{NL}}(X^2 - \sigma^2)) = \int dX P(X) \int \frac{dk}{\sqrt{2\pi}} e^{ik(X + f_{\text{NL}}(X^2 - \sigma^2))} \tilde{f}(k).$$

Expanding the right hand side of the above in a series in f_{NL} , and performing a double Fourier transform, we can write

$$\langle f \rangle = \int dX f(X) \left(P^{(0)}(X) + P^{(1)}(X) + \dots \right).$$

The first term is the expectation value in the absence of f_{NL} given by $P^{(0)}(X) = \frac{1}{\sqrt{2\pi\sigma^2}} \exp\left(-\frac{X^2}{2\sigma^2}\right)$, while the higher order terms may be interpreted as ‘‘corrections’’ to the Gaussian distribution. The first higher order term is obtained as

$$P^{(1)}(X) = -\frac{f_{\text{NL}}\sigma}{\sqrt{2\pi\sigma^2}} e^{-X^2/2\sigma^2} \frac{X(X^2 - 3\sigma^2)}{\sigma^3} \quad (3.1)$$

and the next order is

$$P^{(2)} = \frac{(f_{\text{NL}}\sigma)^2}{\sqrt{2\pi\sigma^2}} e^{-X^2/2\sigma^2} \frac{(X^6 - 11X^4\sigma^2 + 23X^2\sigma^4 - 5\sigma^6)}{2\sigma^6}. \quad (3.2)$$

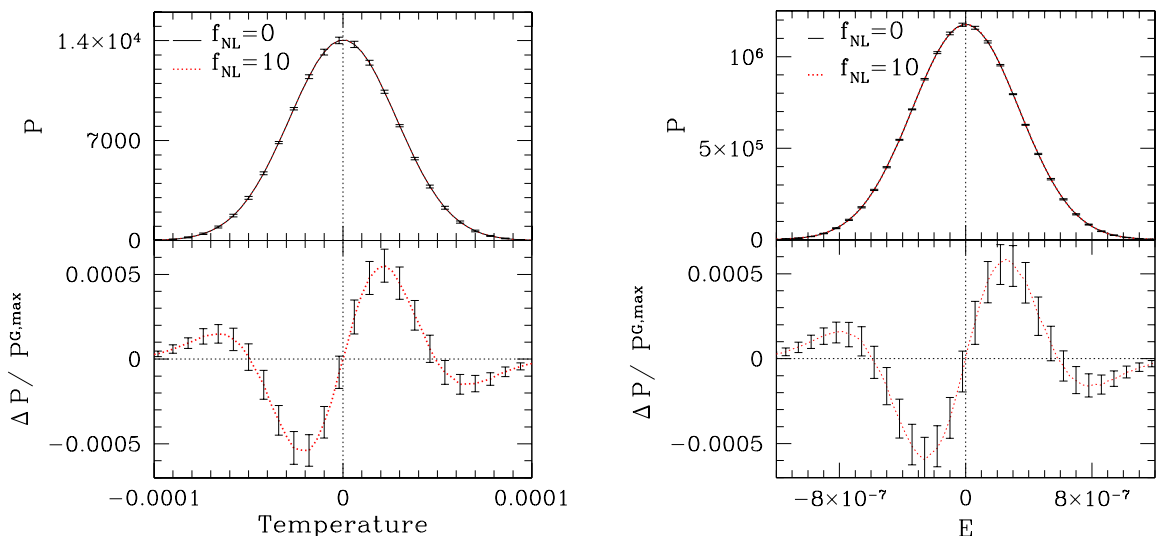


Figure 1. PDF and its non-Gaussian deviation for temperature fluctuations (*left panel*) and E mode (*right panel*) for smoothing angle $\theta_s = 20'$. Plots are average over 1000 simulations. Error bars are the sample variance from the 1000 simulations.

We expect the PDF of ΔT and E to have non-Gaussian deviation of the form given by eq. (3.1) at leading order. The amplitude and the rms however will be modified by the physical events during recombination and subsequent epochs. In the left and right panels of figure 1 we have plotted the normalized PDF for temperature fluctuations and E mode, averaged over 1000 simulations. Upper panels show the PDF for both Gaussian and non-Gaussian cases, while lower panels show ΔP scaled by the amplitude of $P^{(0)}$, for $f_{NL} = 10$. We have used smoothing angle $\theta_s = 20'$. We find that the differences between the Gaussian and non-Gaussian maps in shapes and amplitudes for the two fields are similar, as seen from the lower panels. The shapes are well approximated by eq. (3.1). The second order correction eq. (3.2) is negligible for such small value of f_{NL} .

In figure 1 the non-Gaussian deviation has been calculated between each pair of Gaussian and non-Gaussian maps having the same set of Gaussian $a_{\ell m}$'s. Therefore, a large part of the cosmic variance associated with the fluctuations in the amplitude of harmonic modes are cancelled out and only the part associated with the higher order non-Gaussian term contributes to the sample variances shown in the bottom panel of figure 1. In order to see the full cosmic variance we calculate

$$\Delta P_{i,j}(X) = P(X, i) - P^0(X, j), \quad (3.3)$$

which is the difference between the i -th non-Gaussian and the j -th Gaussian PDFs. There will be 1000×1000 $\Delta P_{i,j}$'s. The mean ΔP over i, j will give the same mean plot shown in the lower panels of figure 1. However, the sample variances will be much larger. We have plotted them in figure 2 showing error bars which are about two orders of magnitude larger than those in figure 1, which confirms our expectations.

The treatment in figure 1 might look unrealistic for a map obtained from real observation because the corresponding Gaussian map is not known. However, in such a situation the Gaussian maps can be created by randomizing the phase of harmonic modes of the observed map while keeping the amplitude of the $a_{\ell m}$'s the same. Here we assume that the smooth-

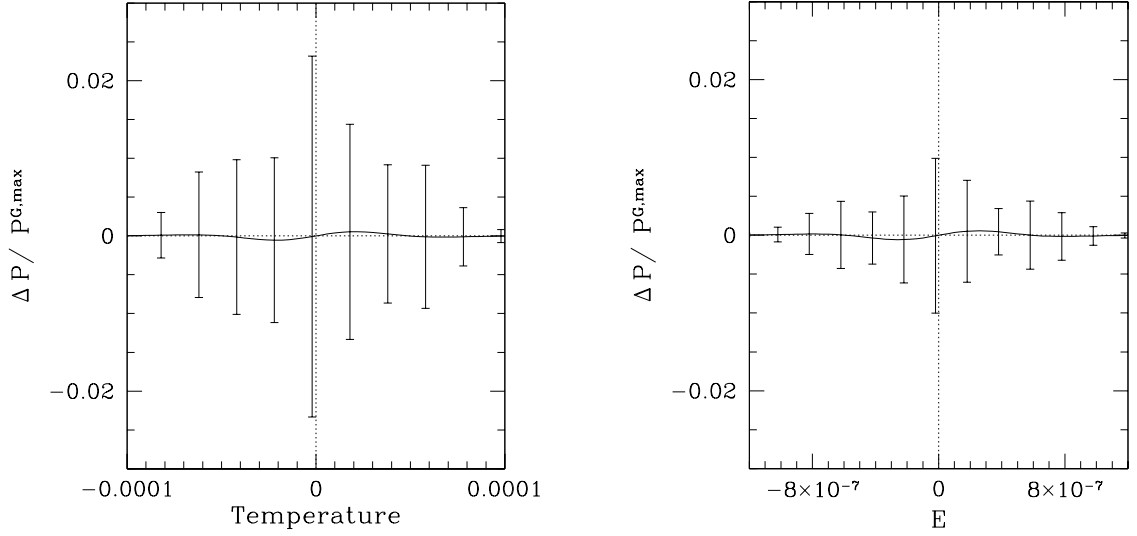


Figure 2. ΔP for T and E (same as the plots in the corresponding lower panels of figure 1) with the error bars being the sample variances calculated using $\Delta P_{i,j}(X)$ given in eq. (3.3).

ing scale is sufficiently small that the resulting temperature or polarization field is a linear combination of many $a_{\ell m}$'s and the Central Limit Theorem applies with uncorrelated $a_{\ell m}$'s. The mean PDFs of the Gaussian maps can be used to calculate the non-Gaussian deviations of the observed map. The observed region can be divided into many subsets to estimate the error bars.

In the next section the non-Gaussian deviations of Minkowski Functionals and Betti numbers are calculated in the same way. Hence the comments made above will be relevant there too.

To calculate the PDF of the total polarization intensity we consider a field of the form $R \equiv \sqrt{X^2 + Y^2}$, where X and Y are independent random variables. We start with the definition

$$P(R, \theta) dR d\theta \equiv P(X) P(Y) dX dY \quad (3.4)$$

where $X = R \cos \theta$, $Y = R \sin \theta$, and integrate over θ . For Gaussian X and Y this gives,

$$P^{(0)}(R) = \frac{R}{\sigma^2} e^{-\frac{R^2}{2\sigma^2}}, \quad (3.5)$$

where the range for R is $[0, \infty)$. For non-Gaussian X and Y of the form given by eq. (2.1) we can use $P(X) = P^{(0)} + P^{(1)} + P^{(2)} + \dots$, where $P^{(1)}$ and $P^{(2)}$ are given by eqs. (3.1) and (3.2) respectively, and substitute in eq. (6) to get the non-Gaussian correction to the PDF for R order by order in $f_{\text{NL}}\sigma$. Because $P^{(1)}(X)$ is odd in X , the PDF for R receives no correction at the first order in $f_{\text{NL}}\sigma$. Then to order $(f_{\text{NL}}\sigma)^2$ the PDF becomes

$$P(R) = \frac{R}{\sigma^2} e^{-\frac{R^2}{2\sigma^2}} \left(1 + \frac{f_{\text{NL}}^2 \sigma^2}{16\sigma^6} (5R^6 - 66R^4 \sigma^2 + 184R^2 \sigma^4 - 80\sigma^6) + \dots \right). \quad (3.6)$$

Thus, we expect smaller non-Gaussian deviations to show up in $I = R$ in comparison to E (since $f_{\text{NL}}\sigma \ll 1$).

Q and U are linearly independent fields and hence the PDF of I , when they are Gaussian, must be of the form eq. (3.5). On the left panel of figure 3 we have plotted the normalized

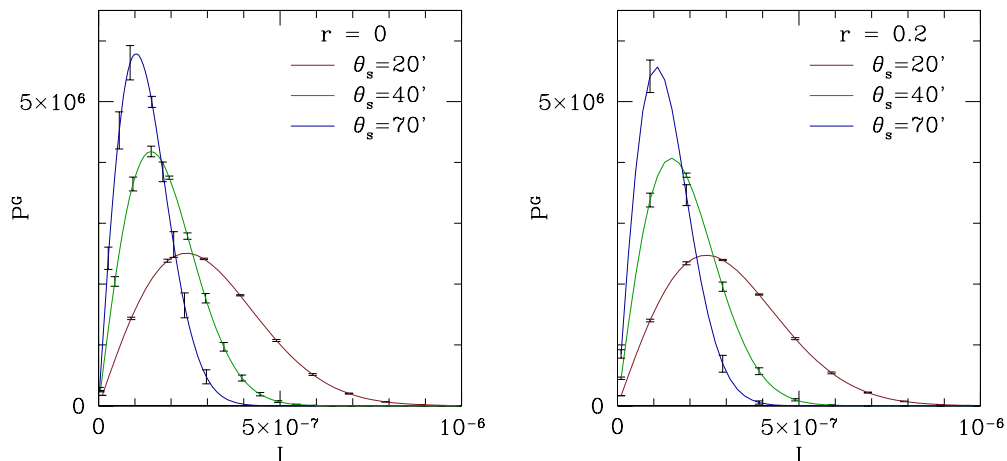


Figure 3. *Left panel:* PDF of Gaussian I where the input E is Gaussian and smoothed with different smoothing angles. The absence of B mode is quantified by the tensor-to-scalar ratio, r , being zero. *Right panel:* the case when Gaussian B mode is present, with $r = 0.2$, and smoothing carried out on the input E and B fields. All plots are average over 1000 simulations and the error bars are their sample variances.

PDF for I for input Gaussian E for different θ_s . The exclusion of B mode corresponds to the value of the tensor-to-scalar ratio, r , being zero. The smoothing was carried out on the input E and then I was constructed from the smoothed fields. The shapes are in agreement with eq. (3.5).

To see the effect of the inclusion of B mode on the PDF of I we have plotted it on the right panel of figure 3 for input Gaussian E and B with tensor-to-scalar ratio $r = 0.2$, for the same smoothing angles as in the left panel. The smoothing was done on the E and B maps. When B mode is included we find that the peak amplitude of the PDF is lower and this becomes distinguishable by eye at larger smoothing angles. Note that only for calculating all the PDFs shown in figure 3 we have used simulations that have input cosmological parameter values obtained from PLANCK [20].

It is important to note that if Gaussian smoothing is carried out on I the PDF shape gets modified by the Gaussian kernel of the smoothing and becomes closer to Gaussian shape in accordance with central limit theorem. But this does not change the fact that the deviation is at $(f_{\text{NL}}\sigma)^2$ order since smoothing is a linear process. In figure 4 we show the PDF and its non-Gaussian deviation for the case where we have taken the simulated E map and performed the smoothing on I and then subtracted the mean. The top panel shows the PDFs for input Gaussian and non-Gaussian E which are difficult to distinguish by eye, while the lower panel shows ΔP scaled by the amplitude of $P^{(0)}$, for $f_{\text{NL}} = 10$. The amplitude of non-Gaussian deviation is about an order of magnitude lower than that of temperature fluctuations and E , and the error bars are about twice larger. For the calculations in the remainder of this paper we will use the variable \tilde{I} with smoothing carried out on I .

4 Geometrical and topological observables

The morphological properties of excursion sets of random fields, which is the set of all points or pixels that have values greater than or equal to a chosen threshold value of the field, can reveal the Gaussian or non-Gaussian nature of the fields. These properties have systematic

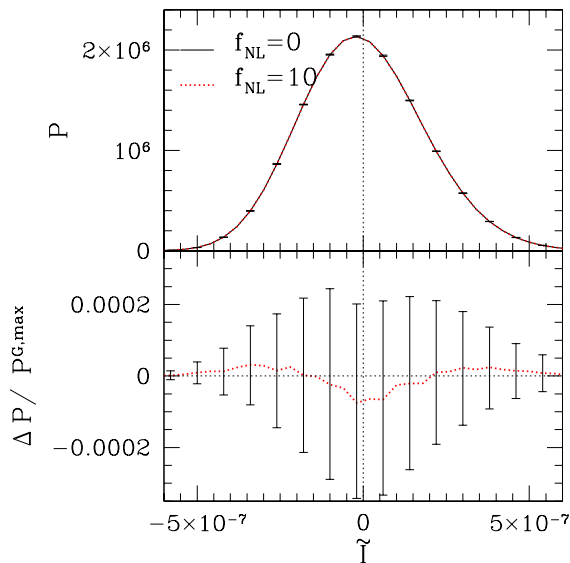


Figure 4. Same as figure 1 for \tilde{I} for input Gaussian and non-Gaussian E , with smoothing done on I .

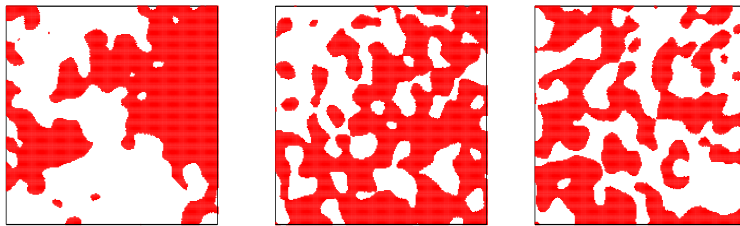


Figure 5. *Left panel:* a $7^\circ \times 7^\circ$ patch of the excursion set for a Gaussian CMB temperature fluctuation field for threshold level $\nu = 0$ and smoothing angle $\theta_s = 90'$. *Middle panel:* the excursion set for E mode for the same sky patch, Gaussian realization, ν and θ_s . *Right panel:* same for \tilde{I} .

behavior as functions of the threshold values that parametrize the excursion sets. We focus here on excursion sets of E and \tilde{I} . For a visual comparison, in figure 5 we show excursion sets (red contiguous regions) for a small patch of the sky for temperature fluctuation (left panel), E mode (middle panel) and \tilde{I} (right panel), for threshold value $\nu = 0$. All three have been obtained from the same input primordial Gaussian fluctuation.

The morphological properties of the excursions sets can be quantified in terms of geometrical and topological quantities namely, the Minkowski Functionals (MFs) and Betti numbers. There are three MFs for two-dimensional manifolds such as the excursion sets of the CMB. The first, denoted by V_0 , is the area fraction of the excursion set. The second, denoted by V_1 , is the total length of iso-temperature contours or boundaries of the excursion set. The third, denoted by V_2 , is the genus which is the difference between the numbers of hot spots and cold spots. For two-dimensional manifolds there are two non-zero Betti numbers, the first, denoted by β_0 , is the number of connected components, while the second denoted by β_1 is the number of holes. (Strictly speaking, for fields on the surface of a sphere β_1 is the number of holes minus one). For the CMB excursion sets β_0 is the number of hot spots and β_1 is the number of cold spots.

For a Gaussian random field the MFs are given by,

$$V_k(\nu) = A_k H_{k-1}(\nu) e^{-\nu^2/2}, \quad k = 0, 1, 2, \quad (4.1)$$

where $H_k(\nu)$ is the k -th Hermite polynomial and the amplitude A_k depends only on the angular power spectrum C_ℓ . It is given by

$$A_k = \frac{1}{(2\pi)^{(k+1)/2}} \frac{\omega_2}{\omega_{2-k}\omega_k} \left(\frac{\sigma_1}{\sqrt{2}\sigma_0} \right)^k, \quad (4.2)$$

$$\sigma_j^2 \equiv \frac{1}{4\pi} \sum_\ell (2\ell+1) [\ell(\ell+1)]^j C_\ell W_\ell^2, \quad (4.3)$$

with $\omega_k \equiv \pi^{k/2}/\Gamma(k/2+1)$. σ_1 is the rms of the gradient of the field and W_ℓ represents the smoothing kernel determined by the pixel and beam window functions and any additional smoothing. For Gaussian smoothing W_ℓ is given by $W_\ell = e^{-\ell(\ell+1)\theta_s^2/2}$.

The presence of any small deviation from Gaussianity will appear as deviations from these Gaussian formulae [14–16]. We denote the non-Gaussian deviation of MFs by

$$\Delta V_i \equiv V_i^{NG} - V_i^G, \quad (4.4)$$

where $i = 0, 1, 2$.

Analytic expressions for Betti numbers are not known even for Gaussian fields. They can be formally expressed as

$$\beta_0 = \frac{1}{2\pi} \int_{C_+} K \, ds, \quad \beta_1 = \frac{1}{2\pi} \int_{C_-} K \, ds, \quad (4.5)$$

where K is the total curvature of iso-temperature contours for each ν . C_+ denotes contours that enclose hot spots while C_- denotes contours that enclose cold spots. Their non-Gaussian deviations are denoted as

$$\Delta\beta_i \equiv \beta_i^{NG} - \beta_i^G, \quad (4.6)$$

where $i = 0, 1$ for Betti numbers.

4.1 Non-Gaussian deviations of Minkowski Functionals

We have calculated MFs numerically following the method given in [47]. It was shown in [48] that this method has an inherent numerical inaccuracy which scales as the square of the finite binning of the threshold values at leading order, arising from the finite approximation of the delta function. This issue is not of concern here for the following reason. For very weakly non-Gaussian case, which is relevant here, the numerical errors of Gaussian and non-Gaussian MFs for the same Gaussian realization are similar and are subtracted off when we calculate the non-Gaussian deviations. We have chosen spacing of ν given by $\Delta\nu = 0.75$ for the range $-4.5 \leq \nu \leq 4.5$.

In the three upper panels of figure 6 we have plotted the MFs and their non-Gaussian deviations for E mode for $f_{\text{NL}} = 10$ for different smoothing angles. Note that the amplitudes scale linearly with f_{NL} . The plots are the average over calculations from 1000 simulations and the error bars are the sample variance over those 1000 simulations. As seen in the panels showing V_1 and V_2 , the contour length and the genus for E have much larger amplitudes in comparison to that of temperature fluctuations (see figure 2 of [15]). This indicates

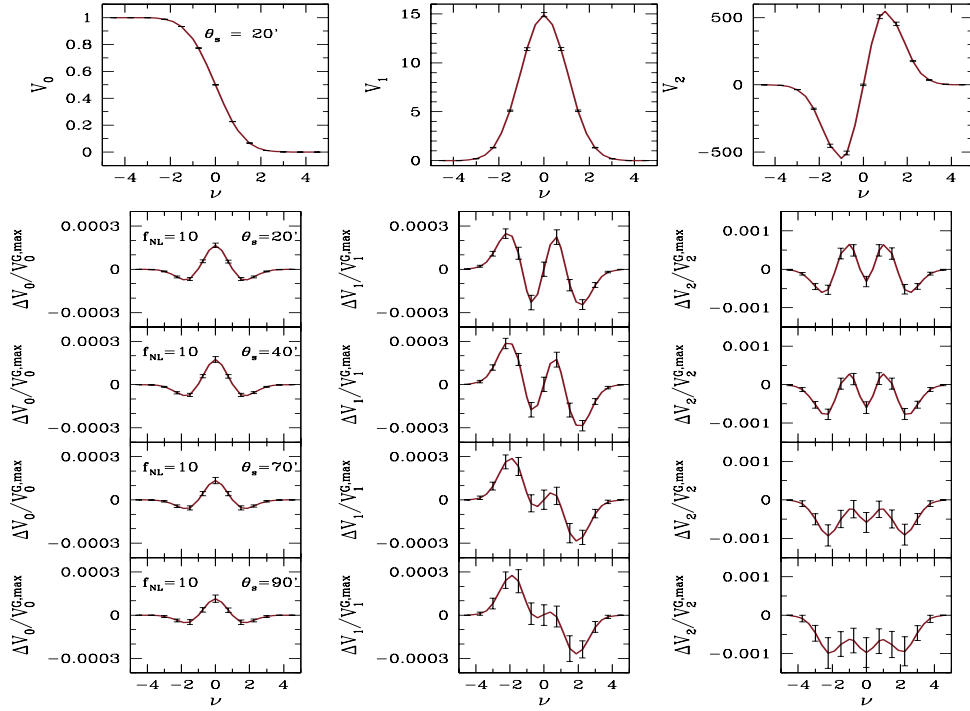


Figure 6. *Upper panels:* MFs for E mode. *Lower panels:* non-Gaussian deviations of MFs for $f_{\text{NL}} = 10$ for different smoothing scales. The error bars are the sample variance from 1000 simulations.

more structure, which may be guessed by visual inspection of figure 5. The non-Gaussian deviations, shown in the lower panels, have characteristic shapes and vary slightly with the smoothing angle. The error bars increase in size as θ_s increases due to loss of statistical significance arising from fewer number of structures. Further, we find that deviations for all three MFs are similar in shape to that of temperature fluctuations and of comparable amplitude. The sizes of error bars are also similar. This implies that E modes carry as much information about non-Gaussian deviations as the temperature fluctuations and hence can be very useful for constraining primordial non-Gaussianity.

Next we look at the MFs for \tilde{I} . In figure 7 we have plotted the MFs (upper panels) and their non-Gaussian deviations for $f_{\text{NL}} = 10$ for different smoothing angles without error bars (middle panels), and the same with error bars (lower panels). The plots are again average over calculations from 1000 simulations and the error bars have been obtained from the same 1000 simulations. The top panels show that the shapes are close to that of Gaussian shapes even though \tilde{I} is not a Gaussian field. The reason is the additional Gaussian smoothing, as discussed in section 3. The amplitude is close to that of E modes at the same smoothing angle. From the middle panels, we see that the shapes of deviations are quite different from that of E . At lower smoothing angles, the deviations amplitudes are much smaller than that of E , and become comparable for the larger ones. Figure 8 shows the same deviations as figure 7 but on a larger scale in order to highlight the large error bars. This implies that statistical fluctuations for non-Gaussian deviations of \tilde{I} are larger than that of E or temperature fluctuations and consequently it has considerably less power to detect local type non-Gaussian model.

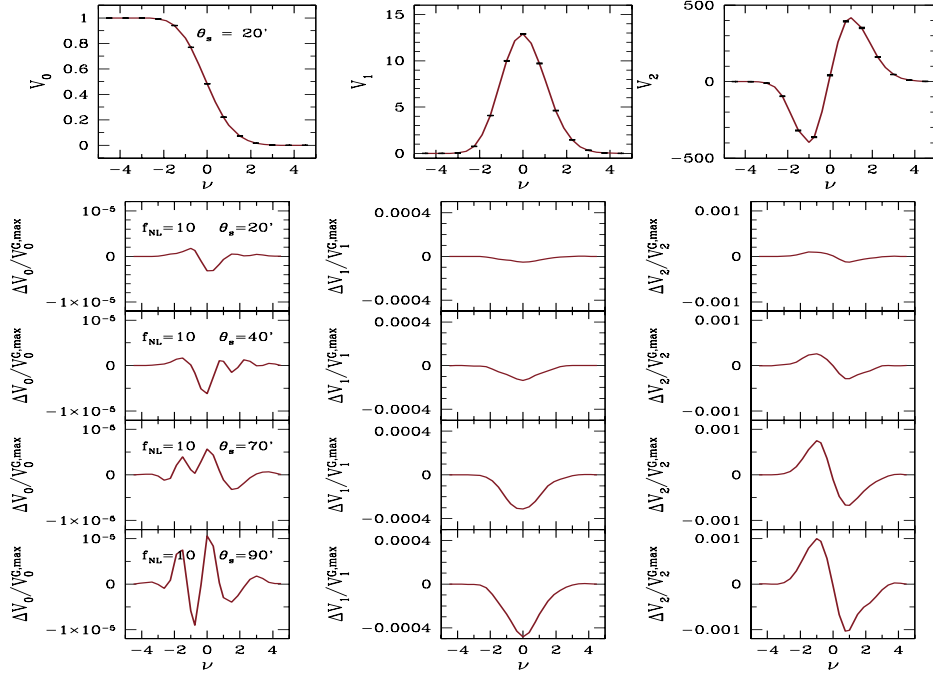


Figure 7. Upper panels: MFs for \tilde{I} . Lower panels: non-Gaussian deviations of MFs for $f_{\text{NL}} = 10$ for different smoothing scales.

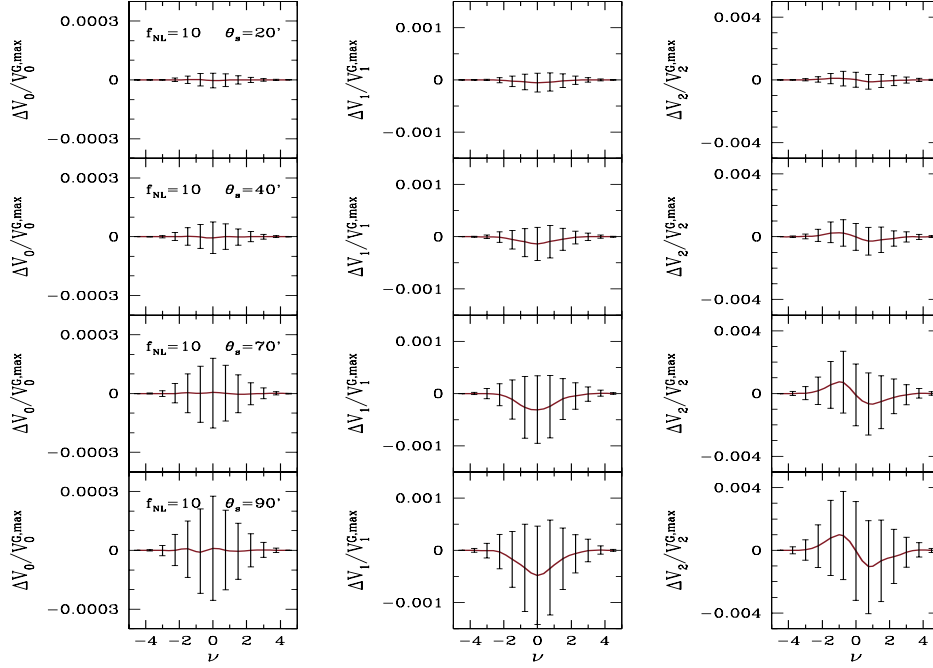


Figure 8. Upper panels: non-Gaussian deviations of MFs for \tilde{I} shown with error bars for the same f_{NL} value and smoothing angles as lower panels of figure 7, but with larger scale to highlight the large size of the error bars. The error bars are the sample variance from 1000 simulations.

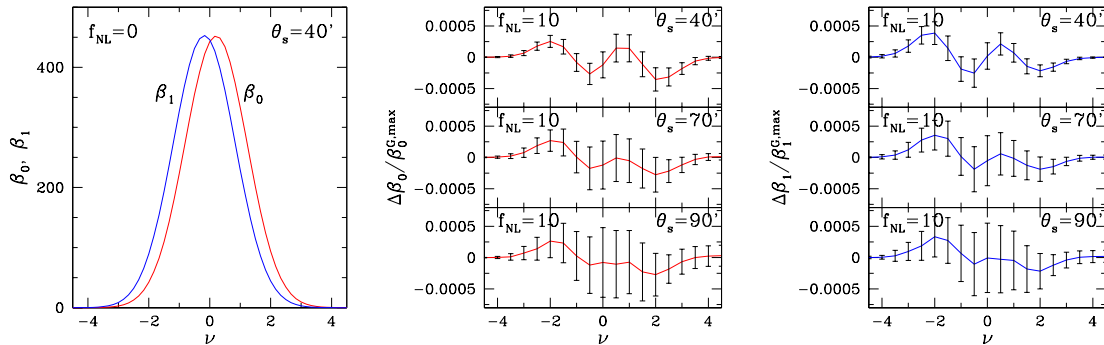


Figure 9. Betti numbers and their non-Gaussian deviations for E , for $f_{\text{NL}} = 10$ and different smoothing angles.

4.2 Non-Gaussian deviations of Betti numbers

For the calculation of Betti numbers we follow the method given in [12, 29]. This method uses a numerical implementation of eq. (4.5). It is based on connecting iso-temperature pixels with the information of the orientation of the contour retained. Contours with the same orientation are then counted to get β_0 and β_1 . We would like to mention that we have not analyzed the accuracy of this technique to the level required by present day resolutions. Hence, though our results are correct qualitatively, we do not use them for accurate statistical analysis or apply it to observational data as yet.

We have used spacing of ν given by $\Delta\nu = 0.5$ for the range $-4.5 \leq \nu \leq 4.5$. Figure 9 shows β_0 and β_1 for Gaussian case (left panel) and their respective non-Gaussian deviations (middle and right panels) for E , averaged over 1000 simulations. The deviation shapes, amplitudes and sizes of error bars are again comparable to that of temperature fluctuations (see figures 3 and 8 of [29]).

Figure 10 shows Gaussian β_0 and β_1 (left panel) and their respective non-Gaussian deviations (middle and right panels) for \tilde{I} , averaged over 1000 simulations. The amplitudes of Gaussian β_0 and β_1 are comparable to those of E . The trend for the amplitudes of non-Gaussian deviations is also similar. They are much smaller for small values of θ_s , and increases as θ_s increases. Figure 11 shows the same deviations as figure 10 but on a larger scale in order to highlight the large error bars. This again implies lower statistical power for \tilde{I} to detect local type non-Gaussianity.

4.3 Comparison of statistical sensitivity of T , E and \tilde{I} to primordial non-Gaussianity

A simple way of estimating the statistical non-Gaussian information encoded in temperature fluctuations, E and \tilde{I} and comparing them, is to integrate the absolute values of the non-Gaussian deviations measured in units of the corresponding sample variances from $\nu = -4.5$ to 4.5. Let us define the quantity A as,

$$A = \Delta\nu \sum_{i=1}^M (|\Delta O(i)| / O^{\text{G,max}}) / \sigma_s(i), \quad (4.7)$$

where M is the number of threshold levels with spacing $\Delta\nu$, O can be either V_1 , V_2 , β_0 or β_1 , and $\sigma_s(i)$ are the respective sample variances at each threshold level i . For Mfs we have $M = 13$.

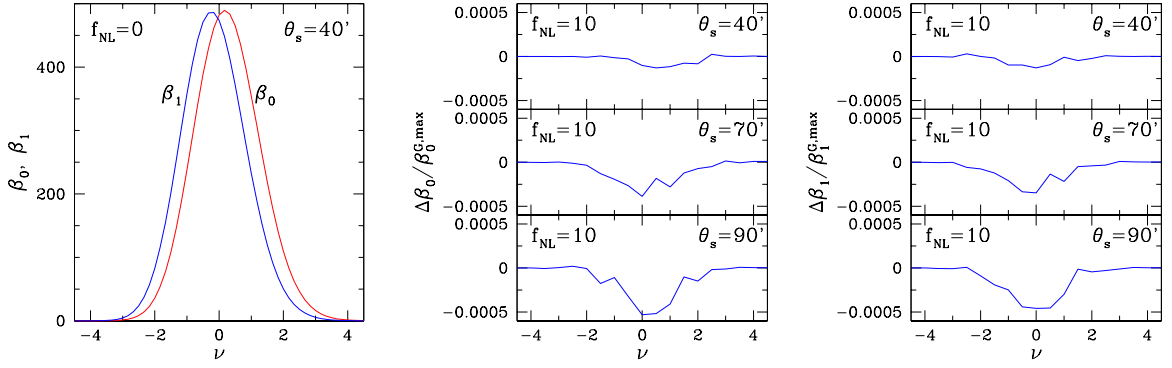


Figure 10. Betti numbers and their non-Gaussian deviations for \tilde{I} , for $f_{\text{NL}} = 10$ and different smoothing angles.

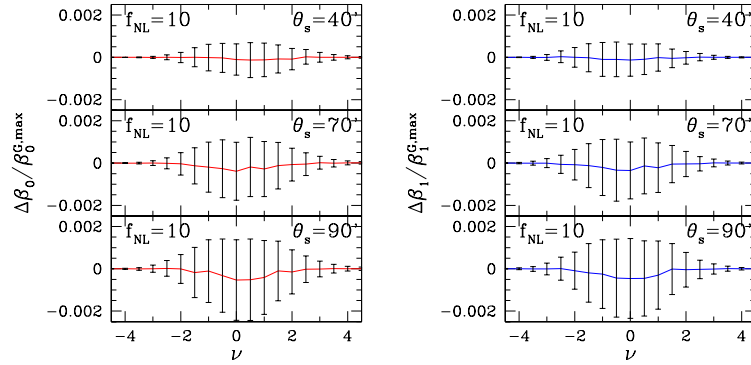


Figure 11. Non-Gaussian deviations of Betti numbers for \tilde{I} with error bars for the same f_{NL} and smoothing angles as figure 10.

Field	Smoothing angle	A for V_1	A for V_2
$\Delta T/T$	$40'$	27.3	22.8
	$70'$	21.3	14.5
	$90'$	18.4	26.0
E	$40'$	34.8	26.0
	$70'$	19.4	19.0
	$90'$	14.0	17.0
\tilde{I}	$40'$	1.2	1.2
	$70'$	1.8	1.6
	$90'$	1.7	1.5

Table 1. Table showing values of A defined in eq. (4.7) for V_1 , V_2 , β_0 and β_1 .

The resulting values are shown in table 1. We find comparable values of A for all four observables (excluding the area fraction) for temperature fluctuations and E . Therefore, we conclude that E can be as useful as temperature fluctuations data for constraining primordial non-Gaussianity. The values of \tilde{I} are however much lower and hence it lacks statistical power for such analysis.

5 Conclusion

In this paper we have investigated the signatures of local type primordial non-Gaussian scalar perturbations on CMB polarization. Such a study has become very important with the availability of increasingly accurate polarization data. To this end we have used local type non-Gaussian simulations of E mode polarization and the total polarization intensity I and calculated non-Gaussian deviations of Minkowski functionals and Betti numbers. Since in our case I is constructed from simulated E mode maps, the non-Gaussian information contained in it is essentially the same as in E . In realistic observational situation I is expected to have contributions from B modes and different systematic instrumental errors can have different signatures in E , B and I . Hence we must analyze all three fields or possibly other clever constructs from them to isolate different sources of non-Gaussianity or check for consistency in the data.

We first derive the expected shapes of PDFs of non-Gaussian E mode and I fields. E mode has deviations of order $f_{\text{NL}}\sigma$, similar to that of temperature fluctuations, as expected. I , on the other hand, has deviations proportional to $(f_{\text{NL}}\sigma)^2$ at the lowest order. Calculations of the PDF and its non-Gaussian deviation from simulated maps for I and confirmed smallness of the amplitude of the non-Gaussian deviation in comparison to that of E . We found that the statistical fluctuations are larger. This implies that I will not be a good field to use for the detection of local-type non-Gaussianity.

Next we analyze the geometrical and topological properties of excursion sets of E and I using Minkowski Functionals and Betti numbers. We find that the non-Gaussian deviations of all the observables for E field is similar in shape, amplitude and size of error bars to that of temperature fluctuations. We conclude that E modes will provide independent and equally strong constraint on f_{NL} . Non-Gaussian deviations of I are much smaller and the error bars are much larger. This is in agreement with what we had obtained for the PDF. So this further implies that I by itself will not constrain f_{NL} well. However, when used in conjunction with E modes, information from I can be extremely valuable in distinguishing different types of non-Gaussianity. For example if we measure the non-Gaussian deviations of MFs from observational data and find that E and I have similar levels of deviations then it will strongly indicate that the source of non-Gaussianity is not f_{NL} type.

In this work we use the clean CMB signal maps and ignored the effects of instrumental noise, beam shape and incomplete sky. It must be noted that instrumental noise levels for polarization in observations such as WMAP are larger than that of temperature fluctuations. This will downgrade the power of polarization map in comparison to the temperature map in constraining f_{NL} in real situations. We are currently investigating this issue. Inclusion of B mode will modify the properties of the total polarization intensity. Recently data from BICEP2 [51] has indicated a rather large value for the tensor-scalar ratio, which translates into a relatively large rms value for B field. Further B modes can carry non-Gaussian information of the primordial tensor perturbations. We are studying these cases in ongoing work and plan to apply the analysis to observational data from PLANCK and other future experiments.

Acknowledgments

The computation required for this work was carried out on the Hydra cluster at IIA. We acknowledge use of the HEALPIX package [52, 53] which was used to derive some of the results. We thank F. Elsner and B. Wandelt for the use of their simulations. P.C. would like to thank Sreedhar B. Dutta for useful discussions.

References

- [1] J.R. Bond and G. Efstathiou, *The statistics of cosmic background radiation fluctuations*, *Mon. Not. Roy. Astron. Soc.* **226** (1987) 655 [[INSPIRE](#)].
- [2] R. Crittenden, R.L. Davis and P.J. Steinhardt, *Polarization of the microwave background due to primordial gravitational waves*, *Astrophys. J.* **417** (1993) L13 [[astro-ph/9306027](#)] [[INSPIRE](#)].
- [3] R.A. Frewin, A.G. Polnarev and P. Coles, *Gravitational waves and the polarization of the cosmic microwave background*, *Mon. Not. Roy. Astron. Soc.* **266** (1994) L21 [[astro-ph/9310045](#)] [[INSPIRE](#)].
- [4] D. Coulson, R.G. Crittenden and N.G. Turok, *Polarization and anisotropy of the microwave sky*, *Phys. Rev. Lett.* **73** (1994) 2390 [[astro-ph/9406046](#)] [[INSPIRE](#)].
- [5] R.G. Crittenden, D. Coulson and N.G. Turok, *Temperature-polarization correlations from tensor fluctuations*, *Phys. Rev. D* **52** (1995) 5402 [[astro-ph/9411107](#)] [[INSPIRE](#)].
- [6] A.A. Starobinsky, *Spectrum of relict gravitational radiation and the early state of the universe*, *JETP Lett.* **30** (1979) 682 [[INSPIRE](#)].
- [7] A.H. Guth, *The Inflationary Universe: A Possible Solution to the Horizon and Flatness Problems*, *Phys. Rev. D* **23** (1981) 347 [[INSPIRE](#)].
- [8] A.A. Starobinsky, *Dynamics of Phase Transition in the New Inflationary Universe Scenario and Generation of Perturbations*, *Phys. Lett. B* **117** (1982) 175 [[INSPIRE](#)].
- [9] A.D. Linde, *A New Inflationary Universe Scenario: A Possible Solution of the Horizon, Flatness, Homogeneity, Isotropy and Primordial Monopole Problems*, *Phys. Lett. B* **108** (1982) 389 [[INSPIRE](#)].
- [10] A. Albrecht and P.J. Steinhardt, *Cosmology for Grand Unified Theories with Radiatively Induced Symmetry Breaking*, *Phys. Rev. Lett.* **48** (1982) 1220 [[INSPIRE](#)].
- [11] H. Tomita, *Curvature Invariants of Random Interface Generated by Gaussian Fields*, *Prog. Theor. Phys.* **76** (1986) 952.
- [12] J.R. Gott, C. Park, R. Juzkiewicz, W.E. Bies, F.R. Bouchet and A. Stebbins, *Topology of microwave background fluctuations — Theory*, *Astrophys. J.* **352** (1990) 1.
- [13] S. Winitzki and A. Kosowsky, *Minkowski functional description of microwave background Gaussianity*, *New Astron.* **3** (1998) 75 [[astro-ph/9710164](#)] [[INSPIRE](#)].
- [14] T. Matsubara, *Statistics of Smoothed Cosmic Fields in Perturbation Theory. 1. Formulation and Useful Formulae in Second Order Perturbation Theory*, *Astrophys. J.* **584** (2003) 1 [[INSPIRE](#)].
- [15] C. Hikage, E. Komatsu and T. Matsubara, *Primordial Non-Gaussianity and Analytical Formula for Minkowski Functionals of the Cosmic Microwave Background and Large-scale Structure*, *Astrophys. J.* **653** (2006) 11 [[astro-ph/0607284](#)] [[INSPIRE](#)].
- [16] T. Matsubara, *Analytic Minkowski Functionals of the Cosmic Microwave Background: Second-order Non-Gaussianity with Bispectrum and Trispectrum*, *Phys. Rev. D* **81** (2010) 083505 [[arXiv:1001.2321](#)] [[INSPIRE](#)].
- [17] C. Hikage, T. Matsubara, P. Coles, M. Liguori, F.K. Hansen and S. Matarrese, *Limits on Primordial Non-Gaussianity from Minkowski Functionals of the WMAP Temperature Anisotropies*, *Mon. Not. Roy. Astron. Soc.* **389** (2008) 1439 [[arXiv:0802.3677](#)] [[INSPIRE](#)].
- [18] C. Hikage and T. Matsubara, *Limits on Second-Order Non-Gaussianity from Minkowski Functionals of WMAP Data*, *Mon. Not. Roy. Astron. Soc.* **425** (2012) 2187 [[arXiv:1207.1183](#)] [[INSPIRE](#)].

- [19] WMAP collaboration, E. Komatsu et al., *Seven-Year Wilkinson Microwave Anisotropy Probe (WMAP) Observations: Cosmological Interpretation*, *Astrophys. J. Suppl.* **192** (2011) 18 [[arXiv:1001.4538](#)] [[INSPIRE](#)].
- [20] PLANCK collaboration, P.A.R. Ade et al., *Planck 2013 Results. XXIV. Constraints on primordial non-Gaussianity*, *Astron. Astrophys.* **571** (2014) A24 [[arXiv:1303.5084](#)] [[INSPIRE](#)].
- [21] P. Chingangbam and C. Park, *Residual foreground contamination in the WMAP data and bias in non-Gaussianity estimation*, *JCAP* **02** (2013) 031 [[arXiv:1210.2250](#)] [[INSPIRE](#)].
- [22] G. Rossi, R.K. Sheth, C. Park and C. Hernandez-Monteagudo, *Non-Gaussian Distribution and Clustering of Hot and Cold Pixels in the WMAP Five-Year Sky*, *Mon. Not. Roy. Astron. Soc.* **399** (2009) 304 [[arXiv:0906.2190](#)] [[INSPIRE](#)].
- [23] G. Rossi, P. Chingangbam and C. Park, *Statistics of the excursion sets in models with local primordial non-Gaussianity*, *Mon. Not. Roy. Astron. Soc.* **411** (2011) 1880 [[arXiv:1003.0272](#)] [[INSPIRE](#)].
- [24] G. Rossi, P. Chingangbam and C. Park, *Excursion Set Statistics with Primordial Non-Gaussianity*, *J. Korean Phys. Soc.* **57** (2010) 563.
- [25] P. Coles and J.D Barrow, *Non-Gaussian statistics and the microwave background radiation*, *Mon. Not. Roy. Astron. Soc.* **228** (1987) 407.
- [26] R. van de Weygaert, E. Platen, G. Vegter, B. Eldering and N. Kruithof, in proceedings of *IEEE International Symposium on Voronoi Diagrams in Science and Engineering (ISVD)*, Quebec, QC, Canada, 28–30 June 2010, pg. 224.
- [27] R. van de Weygaert et al., *Alpha, Betti and the Megaparsec Universe: On the Topology of the Cosmic Web*, *Trans. Comput. Sci. XIV*, in *Lect. Notes Comput. Sci.* **6970** (2011) 60.
- [28] R. van de Weygaert et al., *Probing Dark Energy with Alpha Shapes and Betti Numbers*, [arXiv:1110.5528](#) [[INSPIRE](#)].
- [29] P. Chingangbam, C. Park, K.P. Yogendran and R. van de Weygaert, *Hot and cold spots counts as probes of non-Gaussianity in the CMB*, *Astrophys. J.* **755** (2012) 122 [[arXiv:1206.0436](#)] [[INSPIRE](#)].
- [30] C. Park et al., *Betti numbers of Gaussian fields*, *J. Korean Phys. Soc.* **46** (2013) 125 [[arXiv:1307.2384](#)] [[INSPIRE](#)].
- [31] D. Pogosyan, C. Gay and C. Pichon, *The invariant joint distribution of a stationary random field and its derivatives: Euler characteristic and critical point counts in 2 and 3D*, *Phys. Rev. D* **80** (2009) 081301 [Erratum *ibid.* **D 81** (2010) 129901] [[arXiv:0907.1437](#)] [[INSPIRE](#)].
- [32] D.S. Salopek and J.R. Bond, *Nonlinear evolution of long wavelength metric fluctuations in inflationary models*, *Phys. Rev. D* **42** (1990) 3936 [[INSPIRE](#)].
- [33] T. Falk, R. Rangarajan and M. Srednicki, *The angular dependence of the three point correlation function of the cosmic microwave background radiation as predicted by inflationary cosmologies*, *Astrophys. J.* **403** (1993) L1 [[astro-ph/9208001](#)] [[INSPIRE](#)].
- [34] V. Acquaviva, N. Bartolo, S. Matarrese and A. Riotto, *Second order cosmological perturbations from inflation*, *Nucl. Phys. B* **667** (2003) 119 [[astro-ph/0209156](#)] [[INSPIRE](#)].
- [35] J.M. Maldacena, *Non-Gaussian features of primordial fluctuations in single field inflationary models*, *JHEP* **05** (2003) 013 [[astro-ph/0210603](#)] [[INSPIRE](#)].
- [36] C.-G. Park and C. Park, *Simulation of cosmic microwave background polarization fields for AMiBA experiment*, *J. Korean Astrophys. Soc.* **35** (2002) 67.

- [37] C. Park and C.-G. Park, *Simulation of Cosmic Microwave Background Polarization Fields for AMiBA Experiment*, in *AMIBA 2001: High-z Clusters, Missing Baryons, and CMB Polarization*, L.-W. Chen, C.-P. Ma, K.-W. Ng and U.-L. Pen eds., *ASP Conf. Ser.* **257** (2002) 279.
- [38] S. Galli et al., *CMB Polarization can constrain cosmology better than CMB temperature*, *Phys. Rev. D* **90** (2014) 063504 [[arXiv:1403.5271](#)] [[INSPIRE](#)].
- [39] M. Kamionkowski, A. Kosowsky and A. Stebbins, *Statistics of cosmic microwave background polarization*, *Phys. Rev. D* **55** (1997) 7368 [[astro-ph/9611125](#)] [[INSPIRE](#)].
- [40] M. Zaldarriaga and U. Seljak, *An all sky analysis of polarization in the microwave background*, *Phys. Rev. D* **55** (1997) 1830 [[astro-ph/9609170](#)] [[INSPIRE](#)].
- [41] J. Kovac, E.M. Leitch, C. Pryke, J.E. Carlstrom, N.W. Halverson and W.L. Holzapfel, *Detection of polarization in the cosmic microwave background using DASI*, *Nature* **420** (2002) 772 [[astro-ph/0209478](#)] [[INSPIRE](#)].
- [42] WMAP collaboration, A. Kogut et al., *Wilkinson Microwave Anisotropy Probe (WMAP) first year observations: TE polarization*, *Astrophys. J. Suppl.* **148** (2003) 161 [[astro-ph/0302213](#)] [[INSPIRE](#)].
- [43] F. Elsner and B.D. Wandelt, *Improved simulation of non-Gaussian temperature and polarization CMB maps*, *Astrophys. J. Suppl.* **184** (2009) 264 [[arXiv:0909.0009](#)] [[INSPIRE](#)].
- [44] M. Liguori, S. Matarrese and L. Moscardini, *High-resolution simulations of cosmic microwave background non-Gaussian maps in spherical coordinates*, *Astrophys. J.* **597** (2003) 57 [[astro-ph/0306248](#)] [[INSPIRE](#)].
- [45] P. Chingangbam and C. Park, *Statistical nature of non-Gaussianity from cubic order primordial perturbations: CMB map simulations and genus statistic*, *JCAP* **12** (2009) 019 [[arXiv:0908.1696](#)] [[INSPIRE](#)].
- [46] <http://lambda.gsfc.nasa.gov/product/map/dr3/parameters.cfm>.
- [47] J. Schmalzing and K.M. Gorski, *Minkowski functionals used in the morphological analysis of cosmic microwave background anisotropy maps*, *Mon. Not. Roy. Astron. Soc.* **297** (1998) 355 [[astro-ph/9710185](#)] [[INSPIRE](#)].
- [48] E.A. Lim and D. Simon, *Can we detect Hot or Cold spots in the CMB with Minkowski Functionals?*, *JCAP* **01** (2012) 048 [[arXiv:1103.4300](#)] [[INSPIRE](#)].
- [49] <http://lambda.gsfc.nasa.gov/>.
- [50] http://lambda.gsfc.nasa.gov/product/map/current/m_products.cfm.
- [51] BICEP2 collaboration, P.A.R. Ade et al., *Detection of B-Mode Polarization at Degree Angular Scales by BICEP2*, *Phys. Rev. Lett.* **112** (2014) 241101 [[arXiv:1403.3985](#)] [[INSPIRE](#)].
- [52] K.M. Gorski et al., *HEALPix — A framework for high resolution discretization and fast analysis of data distributed on the sphere*, *Astrophys. J.* **622** (2005) 759 [[astro-ph/0409513](#)] [[INSPIRE](#)].
- [53] <http://healpix.jpl.nasa.gov>.